Geosci. Model Dev., 19, 11189–11207, 2026
https://doi.org/10.5194/gmd-19-11189-2026
© Author(s) 2026. This work is distributed under
the Creative Commons Attribution 4.0 License.

Geoscientific Model Development
Open Access
EGU

Coupling LaMEM 3.0.1 and FastScape 2.8.4 for self-consistent 3D thermo-mechanical and landscape evolution modeling

Yun Luo[1,2], Jianfeng Yang[1,2], Boris J. P. Kaus[3], Anton A. Popov[3], Shaohui Liu[1,2], Xiaoping Yuan[4], and Liang Zhao[5,2]

[1]State Key Laboratory of Lithospheric and Environmental Coevolution, Institute of Geology and Geophysics, Chinese Academy of Sciences, Beijing, 100029, China
[2]College of Earth and Planetary Sciences, University of Chinese Academy of Sciences, Beijing, 100049, China
[3]Institute of Geosciences, Johannes Gutenberg University, Mainz, 55128, Germany
[4]School of Earth Sciences, China University of Geosciences, Wuhan, 430074, China
[5]Key Laboratory of Deep Petroleum Intelligent Exploration and Development, Institute of Geology and Geophysics, Chinese Academy of Sciences, Beijing, 100029, China

Correspondence: Jianfeng Yang (yangjf@mail.iggcas.ac.cn)

Received: 3 March 2026 – Discussion started: 24 March 2026
Revised: 2 November 2026 – Accepted: 17 November 2026 – Published: 24 November 2026

Abstract. The feedback between tectonic events and surface processes shapes both landscapes and lithospheric deformation, yet 3D numerical models that couple thermo-mechanical processes with landscape evolution remain uncommon, partly due to mismatches in temporal and spatial scales between the two. Here, we present a coupling module implemented within LaMEM that couples the thermo-mechanical code LaMEM with the landscape evolution code FastScape. The method transfers surface velocities from the parallel LaMEM grid to a persistent FastScape grid, subdivides each thermo-mechanical timestep into landscape evolution substeps, and returns the updated topography to LaMEM for free-surface and material-phase updates. The module supports 2D and 3D LaMEM configurations, as well as both uniform and non-uniform thermo-mechanical grids. Parameter and resolution tests demonstrate stable behaviour across the investigated buoyancy, bedrock erodibility, hillslope diffusivity, and surface grid settings. A comparison between a 2D-coupled and a fully 3D configuration of a plume-induced dome shows that the 3D model captures the dome-shaped uplift and radial drainage. A 3D subduction model with an oceanic plateau demonstrates the module in a large-scale application with along-strike variability. The source code, input files, and a user manual for the presented tests are archived in a persistent public repository.

1 Introduction

The dynamic interplay between tectonic events, climate, and surface processes fundamentally shapes Earth's topography (Molnar et al., 1993; Beaumont et al., 2001; Whipple, 2009). Crustal deformation via subduction, collision, and mantle dynamics builds surface topography, which in turn influences climate, erosion-deposition processes, and river systems (Clark et al., 2004; Braun, 2010; Castelltort et al., 2012; Sacek et al., 2012; Cloetingh and Willett, 2013; Burov and Gerya, 2014; Replumaz et al., 2020; Yang et al., 2020a; Yuan et al., 2024; Borgohain et al., 2025; Xue et al., 2025). Surface processes may alter the crustal stress field through sedimentary loading and erosional unloading, thereby influencing the dynamics of the orogenic wedge, rifts, and fold-thrust belts (Avouac and Burov, 1996; Burov and Cloetingh, 1997; Willett, 1999; Simpson, 2006; Bishop, 2007; Braun and Yamato, 2010; Vernant et al., 2013; Wolf et al., 2022a; Wolf et al., 2022b; Yang et al., 2023; Li et al., 2025; Zhou et al., 2026). Furthermore, weak and hot materials beneath the surface may move laterally or vertically in response to isostasy. Rapid erosion can promote the upwelling of warmer crustal materials through isostatic adjustment, potentially causing decompression melting and crustal weakening (Beaumont et al., 2001; Zeitler et al., 2001; Koons et al., 2013; Yang et al., 2023). Besides, the loading and unloading of materials (e.g., rock, snow, water) can also cause

spatio-temporal variations in Coulomb stress, which may accelerate or slow the rate of stress loading on active faults and further affect the time intervals between seismic events (Gao et al., 2000; Heki, 2003; Bettinelli et al., 2008; Liu et al., 2009; Steer et al., 2014).

There are increasing reports of interactions among tectonic, climate, and landscape systems; however, our quantitative understanding of these interactions remains limited. Numerical models have played a pivotal role in quantifying these couplings. Previous studies have integrated surface processes and tectonics to examine the evolution of convergent systems (Burov, 2007; Braun and Yamato, 2010), folding (Simpson, 2006; Collignon et al., 2014), rifting and faulting systems (Sacek et al., 2012; Andrés-Martínez et al., 2019; Theunissen and Huismans, 2019; Wolf et al., 2022a), subduction processes (Munch et al., 2022), and mountain belts (Willett, 1999; Thieulot et al., 2014; Ueda et al., 2015; Wolf et al., 2022b) through both 2D and 3D models. Fully 3D coupled models have already been demonstrated in previous studies (e.g., Braun and Yamato, 2010; Thieulot et al., 2014; Ueda et al., 2015; Munch et al., 2022; Neuharth et al., 2022; Wolf et al., 2022a; Wolf et al., 2025; Lu et al., 2026). Beyond a particular code combination, documented coupling procedures and numerical tests can inform the development and assessment of three-dimensional coupled models. Such models are particularly important when tectonic forcing, lithospheric structure, topographic uplift, and drainage evolution vary along strike. Examples include deformation around finite-width indenters, fault-controlled landscapes, localized mantle upwelling, segmentation of subduction zones, and the interaction of subduction with buoyant oceanic plateaus (e.g., Burov and Gerya, 2014; Chen et al., 2017; Yang et al., 2020b; Sun et al., 2021; Maiti et al., 2024). Nevertheless, coupling lithospheric-scale thermo-mechanical models with landscape evolution models presents several numerical challenges. The two model components operate at different spatial and temporal scales. On the spatial scale, landscape evolution models commonly resolve domains of tens to hundreds of kilometers, with grid spacing of tens to hundreds of meters (Stock and Dietrich, 2006; Braun and Willett, 2013; Olive et al., 2014; Thieulot et al., 2014; Willett et al., 2014). In contrast, thermo-mechanical models are suited to much larger scales, spanning hundreds to thousands of kilometers, and typically operate at lower resolution than landscape models (Pusok and Kaus, 2015; Yang et al., 2020b; Stanković et al., 2023; Maiti et al., 2024). Their grid structures may also differ, requiring consistent transfer of surface velocities and topography between uniform or non-uniform thermo-mechanical grids and a regular landscape grid. On the temporal scale, thermo-mechanical models usually adopt larger timesteps, ranging from a thousand to ten thousand years, whereas landscape evolution models use much smaller timesteps, which may require subdividing the thermo-mechanical timestep into multiple landscape evolution substeps in coupled models (Ueda et al., 2015). Horizontal advection presents an additional numerical challenge because errors in transporting topography can smooth topographic gradients and alter drainage organization, particularly when surface displacement is large relative to the landscape-grid spacing.

Here, we present a coupling module that integrates the 3D thermo-mechanical code LaMEM with the landscape evolution code FastScape. We document its design and assess it using decoupled end-member benchmarks, resolution and parameter tests, and a comparison of alternative horizontal advection treatments. Although the current implementation is developed for LaMEM and FastScape, these design and verification procedures are relevant to other coupled thermo-mechanical and landscape evolution models, providing documented coupling procedures and reproducible verification test cases. Section 2 describes the two components of the coupling module and the coupling design, including grid generation, data exchange, time stepping, and an improved horizontal advection method. Section 3 verifies the implementation with two new decoupled end-member tests, compares a 2D-coupled configuration with a fully 3D configuration, presents parameter sensitivity tests, and demonstrates the module in a 3D subduction model with an oceanic plateau. Section 4 discusses the computational performance, limitations, and scope of applicability of the approach.

2 Method

We integrated the 3D parallel thermo-mechanical numerical code LaMEM (Kaus et al., 2016; version 3.0.1) with the landscape evolution code FastScape (Braun and Willett, 2013; Yuan et al., 2019; Fortran-based version 2.8.4) through a coupling module. This module is implemented within the LaMEM source tree, and FastScape is compiled as a library and called through its Fortran interface. All coupling options, including the surface-process parameters, are specified in the standard LaMEM input file. The module supports the uniform and non-uniform grid schemes available in LaMEM. LaMEM additionally offers dynamic grids in which the grid spacing varies with compression or extension, but this option is not recommended for coupled runs because regridding disrupts the drainage network (see Sect. 4). In coupled runs, the velocity field driving the landscape evolution model is computed by the thermo-mechanical model at every timestep, rather than being prescribed as a constant or an analytical function. Section 2.1 summarizes the thermo-mechanical model, Sect. 2.2 summarizes the landscape evolution model, and Sect. 2.3 describes the coupling module in detail.

2.1 Thermo-mechanical model

LaMEM (Kaus et al., 2016) is a 3D thermo-mechanical numerical code that employs a marker-in-cell method to

track material properties and to implement material advection within an Eulerian kinematic framework. It solves the governing equations of momentum, mass, and energy conservation (1)–(3) using a multigrid approach:

$$-\frac{\partial P}{\partial x_i}+\frac{\partial \tau_{ij}}{\partial x_j}+\rho g_i=0, \tag{1}$$

$$\frac{1}{K}\frac{\mathrm{D}P}{\mathrm{D}t}-\alpha\frac{\mathrm{D}T}{\mathrm{D}t}+\frac{\partial v_i}{\partial x_i}=0, \tag{2}$$

$$\rho C_p\left(\frac{\mathrm{D}T}{\mathrm{D}t}\right)=\frac{\partial}{\partial x_i}\left(\lambda\frac{\partial T}{\partial x_i}\right)+H, \tag{3}$$

where g_i are components of gravitational acceleration, P is pressure, ρ is density, τ_{ij} are components of the deviatoric stress tensor, K is the bulk modulus, α is the thermal expansion coefficient, v_i are components of velocity, C_p is the effective isobaric heat capacity, λ is thermal conductivity, H is the volumetric heat source, and $\frac{\mathrm{D}}{\mathrm{D}t}$ is the substantial time derivative.

The code incorporates the visco-elasto-plastic rheology, where the deviatoric strain rate consists of the following components:

$$\dot{\epsilon}_{ij}=\dot{\epsilon}_{ij}^{\mathrm{el}}+\dot{\epsilon}_{ij}^{\mathrm{diff}}+\dot{\epsilon}_{ij}^{\mathrm{disl}}+\dot{\epsilon}_{ij}^{\mathrm{pl}}=\frac{\hat{\tau}_{ij}}{2G}+\eta_{\mathrm{diff}}\tau_{ij}+\eta_{\mathrm{disl}}(\tau_{\mathrm{II}})^{n-1}+\dot{\lambda}\frac{\partial Q}{\partial \sigma_{ij}}, \tag{4}$$

where $\dot{\epsilon}_{ij}^{\mathrm{el}}$, $\dot{\epsilon}_{ij}^{\mathrm{diff}}$, $\dot{\epsilon}_{ij}^{\mathrm{disl}}$, $\dot{\epsilon}_{ij}^{\mathrm{pl}}$ are the elastic, diffusion, dislocation, and plastic strain rate, respectively. G is the elastic shear modulus, $\hat{\tau}_{ij}=\frac{\partial \tau_{ij}}{\partial t}+\tau_{ik}\omega_{kj}-\omega_{ik}\tau_{kj}$ is the Jaumann objective stress rate, $\omega_{ij}=\frac{1}{2}\left(\frac{\partial v_i}{\partial x_j}-\frac{\partial v_j}{\partial x_i}\right)$ is the spin tensor. η_{diff} and η_{disl} are diffusion and dislocation constants, respectively. n is the power-law exponent for dislocation creep. τ_{II} is the square root of the second invariant of the deviatoric stress tensor. $\dot{\lambda}$ is the magnitude of the plastic strain rate, and Q is the plastic flow potential (e.g., Moresi et al., 2007; Popov et al., 2025).

The creep flow law follows:

$$\eta_{\mathrm{diff,disl}}=\frac{1}{2}(\dot{\epsilon}_{\mathrm{II}})^{\frac{1-n}{n}}(B_{\mathrm{N}})^{-\frac{1}{n}}\exp\left(\frac{E+PV}{nRT}\right), \tag{5}$$

where $\dot{\epsilon}_{\mathrm{II}}=\sqrt{0.5\dot{\epsilon}_{ij}^{\mathrm{vis}}\dot{\epsilon}_{ij}^{\mathrm{vis}}}$ is the second invariant of the viscous strain rate tensor. B_{N}, E, V, n are experimentally determined flow law parameters, which represent the pre-factor, stress exponent of dislocation creep, activation energy, and activation volume, respectively. R is the gas constant, P is the pressure, and T is the temperature.

Rock fails when the stress exceeds the yield stress (i.e., $\tau_{\mathrm{II}}\geq\tau_{\mathrm{y}}$), which follows the Drucker-Prager yielding criterion:

$$\tau_{\mathrm{y}}=P\sin(\theta)+C\cos(\theta), \tag{6}$$

where τ_{y} is the yield stress, C is the cohesion, θ is the effective friction angle, and P is the pressure.

Within each computational cell, the effective viscosity (η_{eff}) for nonlinear visco-elasto creep rheology is computed by numerically solving the scalar equation $r(\eta_{\mathrm{eff}})$ using a bisection method (Popov and Sobolev, 2008):

$$r(\eta_{\mathrm{eff}})=\dot{\epsilon}_{\mathrm{II}}^{*}-\frac{\tau_{\mathrm{II}}}{2G\Delta t}-\eta_{\mathrm{diff}}\tau_{\mathrm{II}}-\eta_{\mathrm{disl}}(\tau_{\mathrm{II}})^{n}, \tag{7}$$

$$\tau_{\mathrm{II}}=2\eta_{\mathrm{eff}}\dot{\epsilon}_{\mathrm{II}}^{*}, \tag{8}$$

The effective strain rate ($\dot{\epsilon}_{ij}^{*}$) incorporates a term resulting from advected and rotated deviatoric history stress from the previous time step (τ_{ij}^{*}) as follows:

$$\dot{\epsilon}_{ij}^{*}=\dot{\epsilon}_{ij}+\frac{\tau_{ij}^{*}}{2G\Delta t}, \tag{9}$$

History stresses are advected via markers, followed by distance-based averaging of stress components within the control volumes of the staggered grid. Stress rotation is implemented through numerical integration of the Jaumann objective stress rate, ensuring asymptotically correct results for large finite time steps (Thielmann et al., 2015; Gerya, 2019).

When plastic failure occurs, the effective viscosity is directly computed through:

$$\eta_{\mathrm{eff}}=\frac{\tau_{\mathrm{y}}}{2\dot{\epsilon}_{\mathrm{II}}^{*}}, \tag{10}$$

LaMEM can handle the free surface condition and large-scale lithospheric deformation as shown in previous studies (e.g., Pusok et al., 2018; Yang et al., 2020b; Sun et al., 2021; Wang et al., 2021; Moulas et al., 2022). A layer of low-viscosity, low-density "sticky air" overlies the rocks, and LaMEM additionally tracks the rock-air interface as an internal free surface, represented by a 2D grid of surface elevations. This combination approximates a stress-free boundary within the finite-difference scheme while allowing large, stable timesteps through a free-surface stabilization algorithm (Kaus et al., 2010). The internal free surface defines the topography h that is exchanged with the landscape evolution model. In standalone LaMEM runs, the free surface is advected with the local velocity field, whereas in coupled runs, this advection is delegated entirely to the landscape evolution model, as described in Sect. 2.3. Material properties are updated according to the positions of markers relative to the free surface. Markers of rock phases located above the surface are converted to the air phase, which realizes erosion, and air markers located below the surface are converted to a sedimentary rock phase whose properties are prescribed in the input file, which realizes deposition.

2.2 Landscape evolution model

Based on the assumption that water flows down the path of the steepest slope, FastScape determines the order in which

one must go through the nodes. Through an implicit Euler finite-difference scheme, FastScape can efficiently and stably solve the equation governing long-term fluvial erosion and sediment deposition (Braun and Willett, 2013; Yuan et al., 2019). The rate of topographic change responds to tectonic uplift, river erosion, and sediment deposition, which combine stream power erosion and sediment transport phenomena:

$$\frac{\partial h}{\partial t} = U - K_{\mathrm{f}} \tilde{p}^m A^m S^n + \frac{G}{\tilde{p} A} \int_A \left(U - \frac{\partial h}{\partial t} \right) \mathrm{d}A, \tag{11}$$

where h is topography, U is the rock uplift rate, A is the upstream catchment area (drainage area), S is the slope, m and n are the stream power exponents, and K_{f} is the bedrock erodibility. The dimensionless $\tilde{p}$ parameter represents any spatial or temporal variation in precipitation p relative to the mean precipitation rate. G is a non-dimensional deposition coefficient.

A linear diffusion term gives the hillslope processes:

$$\frac{\partial h}{\partial t} = K_{\mathrm{d}} \nabla^2 h, \tag{12}$$

where h is topography, K_{d} is the transport coefficient for hillslope diffusion.

For the fluvial part (Eq. 11), an implicit Euler scheme discretizes the equation, with the integral term replaced by a sum over upstream nodes. A Gauss-Seidel iterative method is included to solve the resulting nonlinear system with $O(N)$ complexity (Yuan et al., 2019). The diffusion term (Eq. 12) is addressed separately using an alternating direction implicit and $O(N)$ scheme (Peaceman and Rachford, 1955).

2.3 The coupling module

The coupling module integrates LaMEM and FastScape by exchanging and storing the necessary geomorphic data. At initialization, the material composition field in LaMEM is set up, and a surface grid in FastScape is created based on the surface grid used in LaMEM. At each time step, LaMEM first solves the thermo-mechanical equations. The surface velocities are then transferred to FastScape, which subdivides the thermo-mechanical timestep (typically) into smaller timesteps, advects the topography in both horizontal and vertical directions on the surface, and solves the surface processes. Once landscape evolution is complete, the updated topography field is interpolated back into LaMEM, and the marker phases are updated accordingly (Fig. 1a).

The module comprises three key components: (a) generating the initial surface grid based on the grid type used in LaMEM during the initialization stage (Fig. 1b); (b) collection and distribution of data between the parallel LaMEM ranks and the serial FastScape process, which runs on rank 0 (Fig. 1c); and (c) transfer of information between the two grids (Fig. 1d).

During initialization, adjustments to FastScape are required because LaMEM offers combinations of non-uniform and uniform grids in both 2D and 3D, yielding four possible configurations. The initial FastScape grid is generated in a fixed sequence. The module first determines whether the thermo-mechanical grid is 3D, then assesses its uniformity, and finally applies any user-defined refinement (Fig. 1b). For a 2D thermo-mechanical model, whose surface is a 1D line in LaMEM, an extended length is introduced in the second horizontal direction to form the x-y surface required by FastScape. The extended length is also a user-defined parameter in the input file. For non-uniform LaMEM grids, FastScape utilizes the minimum spacing in LaMEM to generate a higher-resolution uniform rectangular grid. During the refinement assessment, a refinement factor n is applied, prompting the insertion of $n - 1$ points at equal intervals between LaMEM's original grid nodes. Consequently, the grid resolution is enhanced by the refinement factor n in both the x and y directions. Once initialization is complete, the FastScape grid remains unchanged for the entire simulation, so the organization of the landscape into valleys, hillslopes, and ridges, which has a response time of up to several Myr, is never disrupted by re-gridding.

Due to the complexity of thermo-mechanical equations, LaMEM employs PETSc-based parallelization for high-performance cluster computing, while FastScape operates serially. An information transceiver gathers data from the parallel LaMEM ranks onto the primary rank, which executes FastScape (Fig. 1c). Only the values at the surface grid nodes are gathered, not the full 3D fields, so the communication volume scales with the number of surface nodes rather than the domain size.

The velocity and topography parameters (v_x, v_y, v_z, h) are exchanged between LaMEM and FastScape at the surface grid nodes. FastScape receives topography from LaMEM once, at the first coupling step of the simulation. After that, it retains its own topography field between coupling steps, and only the velocity field is re-imported from LaMEM at every timestep. This prevents the artificial drainage reorganization that would result from re-initializing the topography from the coarser LaMEM grid at each timestep. After the landscape calculation, the updated topography field is returned to LaMEM. Given that there might be differences between the surface grids of LaMEM and FastScape, we follow a similar procedure to transfer information between the two: first, determine whether the LaMEM grid is 2D. Then, determine whether the LaMEM grid is non-uniform or the FastScape grid is refined. For a 2D thermo-mechanical model, all initialization values in FastScape are set based on this principle: Each value on a line perpendicular to the original line in LaMEM is assigned the value of the corresponding point on the original line in LaMEM. After completing the geomorphic evolution at this time step, the average value along the extended line is calculated and returned to the corresponding grid in LaMEM. In cases where non-uniform or refined

grids are used, values are transferred bidirectionally using bilinear interpolation based on the values of four nearest nodes (Fig. 1d).

During coupled runs, all advection of the topography is performed within FastScape. The internal free-surface advection of LaMEM is disabled, so that no displacement is applied twice. Because the stable timestep of the landscape evolution model is much smaller than the thermo-mechanical timestep Δt_{TM} (typically 10^3 to 10^4 years), each Δt_{TM} is subdivided for the surface-process calculation. The FastScape timestep is set to $\Delta t_{\mathrm{FS}} = \min(\Delta t_{\mathrm{TM}}, \Delta t_{\mathrm{user}})$, where Δt_{user} is the user-defined maximum landscape timestep, and FastScape performs $N = \Delta t_{\mathrm{TM}}/\Delta t_{\mathrm{FS}}$ sub-steps of equal length $\Delta t_{\mathrm{TM}}/N$ within each thermo-mechanical step. In practice, we find that large uplift rates or horizontal surface velocities may result in false parallel rivers during horizontal advection due to numerical diffusion. We thus use an alternative horizontal advection method known as the Back and Forth Error Compensation and Correction (Liu et al., 2005; Kim et al., 2007) within our coupling module and made modifications to parts of the original FastScape code. Figure 2 shows the reproduction results of the same topographic field by two different advection methods. Users can choose the original FastScape or our modified FastScape advection code according to their own needs.

In summary, one coupling step proceeds as follows. (1) LaMEM solves the thermo-mechanical equations and advances by Δt_{TM}. (2) The surface velocities are gathered onto the primary rank and interpolated onto the FastScape grid. (3) The number of sub-steps N is determined from Δt_{TM} and Δt_{user}. (4) FastScape advects the topography with the surface velocity field and solves fluvial erosion, deposition, and hillslope diffusion over N sub-steps. (5) The updated topography is restricted to the LaMEM grid and distributed back to all ranks. (6) The internal free surface is updated, and markers are converted between rock, air, and sediment phases according to their position relative to the new surface.

The total rock and sediment mass need not remain constant in coupled simulations because surface processes can transport sediment across the model boundaries. Sediment leaving an open lateral boundary represents a physical boundary flux and is removed from the landscape evolution domain, which does not directly remove mass from the internal thermo-mechanical system. In addition, the present data-transfer procedure is not strictly conservative, so interpolation, downsampling, and averaging may introduce small numerical changes in integrated topographic or sediment volumes. These boundary fluxes and grid-transfer effects should be distinguished when assessing the mass budget. A fixed boundary results in a loss of mass considered as sediment discharge, while a reflective boundary prevents sediment export through the boundary.

3 Model verification and example applications

We use three groups of models to verify and demonstrate our coupled code. We first verify that the coupling correctly solves the equations and then evaluate and demonstrate its behavior in geodynamic applications. First, two decoupled end-member tests isolate each component and confirm that the coupling machinery neither perturbs the thermo-mechanical solution nor corrupts the landscape solution (Sect. 3.1). Second, plume models compare a 2D coupled configuration with a fully 3D coupled configuration and test the sensitivity of the results to thermo-mechanical and surface-process parameters (Sect. 3.2). Third, a 3D subduction model with an oceanic plateau demonstrates the module in a large-scale tectonic application with lateral variability (Sect. 3.3). Models with and without surface processes are shown for comparison when relevant.

3.1 Coupling interface verification end-member tests

To verify the accuracy of the coupling module, we present two end-member tests in which one of the two components is effectively inactive. In the first test, referred to as NoFSModel, a coupled falling-block model is run with a negligibly small erosion rate, so that the surface-process calculation should not modify the topography produced by the thermo-mechanical model. Its results are compared with those from a standalone LaMEM run using the same setup. In the second test, referred to as NoLMModel, the data transfer from LaMEM to FastScape is disabled, and a constant uplift rate is prescribed directly in FastScape, so the landscape evolution should be unaffected by the presence of the thermo-mechanical model. Its results are compared with those from a standalone FastScape run using the same setup. Together, the two tests verify that the data pathways of the coupling module reproduce the solutions of each component code.

3.1.1 Initial model setup

For the NoFSModel, the model domain is $100\,\mathrm{km} \times 100\,\mathrm{km} \times 120\,\mathrm{km}$ (Fig. 3a), resolved by $48 \times 48 \times 48$ cells. A rigid block is included in this model, which is located at 40 to 60 km in the x-direction and -40 to -20 km in the z-direction (Fig. 3b). All rheological parameters used in the models are listed in Table 1. The model is free-slip for all boundaries except the free-surface top boundary. A 20 km-thick "sticky-air" layer is used to mimic the internal free-surface condition in the finite difference scheme. The thermo-mechanical side boundaries have zero heat flux. FastScape uses the same domain as the tectonic model ($100\,\mathrm{km} \times 100\,\mathrm{km}$), at the same resolution (48×48 cells). The bedrock erodibility K_{f} is set to the negligibly small value of $1 \times 10^{-20}\,\mathrm{m}^{0.2}\,\mathrm{yr}^{-1}$, and the transport coefficient K_{d} to $1 \times 10^{-10}\,\mathrm{m}^2\,\mathrm{yr}^{-1}$ so that surface processes are effectively switched off while the full coupling

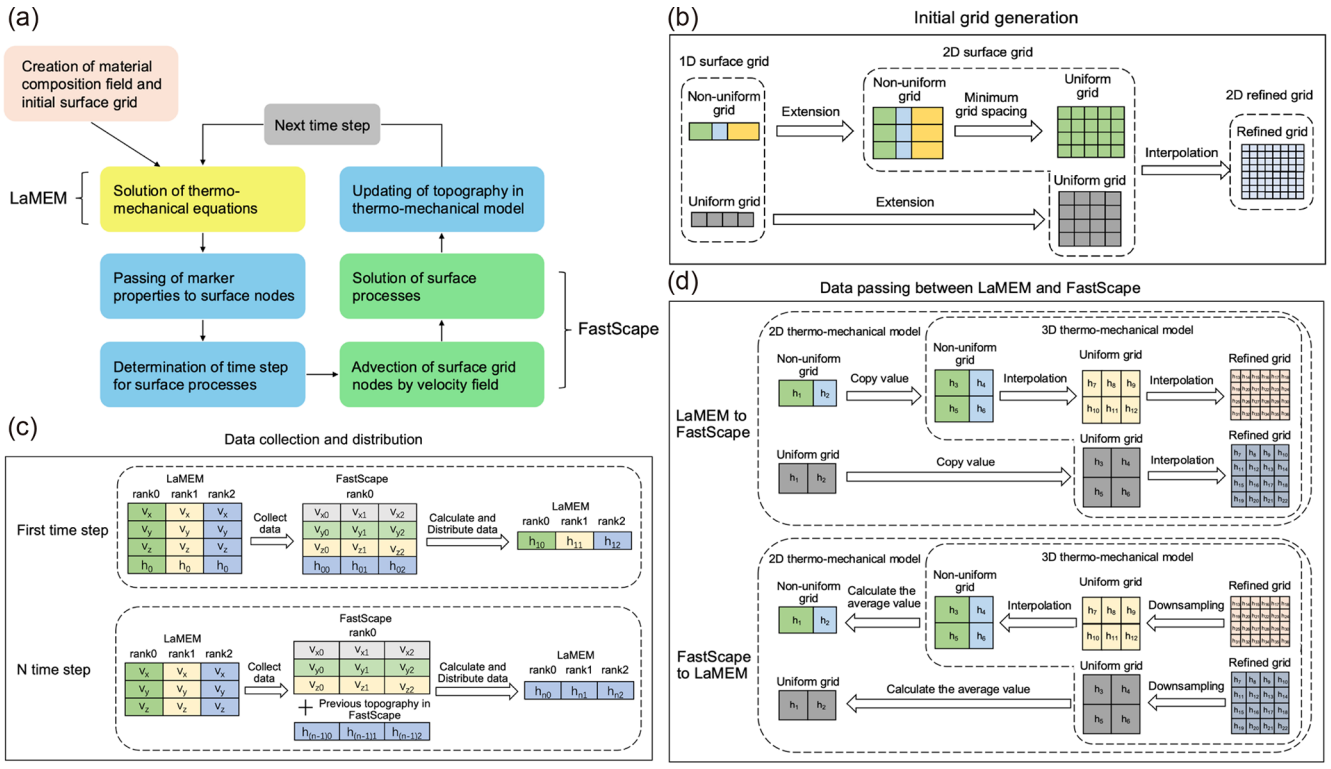


Figure 1. Workflow of the coupling module. **(a)** Flow chart for coupled computation with synchronous stepping. Steps with yellow background: thermo-mechanical calculation; green: surface processes calculation; blue: coupling module calculation; pink: model initialization stage. **(b)** Initial grid generation. For the 2D thermo-mechanical model whose surface is a 1D line in LaMEM, the surface grid is first extended in the second horizontal direction to form the x-y surface required by FastScape (left branch). For the 3D thermo-mechanical model, the procedure starts directly from its 2D surface grid (middle branch). Non-uniform grids are converted to the uniform rectangular grid required by FastScape using the minimum grid spacing in LaMEM, and the grid can then be refined by a factor n through bilinear interpolation to achieve higher precision in the geomorphic evolution. **(c)** Data collection and distribution between the parallel LaMEM ranks and the serial FastScape process. Only the surface-node values are gathered on rank 0, which executes FastScape and redistributes the updated topography to all ranks. At the first time step, both the velocities and the topography are collected, whereas at all subsequent time steps, only the velocities are collected, and FastScape reuses the topography stored from the previous step without re-interpolating from the coarse mesh of LaMEM. **(d)** Data transfer between LaMEM and FastScape grids for different grid types. Values passed from LaMEM to FastScape are obtained by copying or bilinear interpolation. Values returned from FastScape to LaMEM are obtained by downsampling to the LaMEM resolution, followed by interpolation onto non-uniform grids where required, or by averaging along the extension direction for 2D models. In the 2D thermo-mechanical model, the values along the extended direction at the same line are identical. For example, in the transfer from LaMEM to FastScape within the 2D non-uniform grid, $h_3 = h_5$ and $h_4 = h_6$. However, these values differ in the 3D thermo-mechanical model.

remains active. All FastScape boundaries are open, allowing sediment flux to leave the domain.

For the NoLMModel, the velocity and topography of the thermo-mechanical model are not passed to FastScape. Instead, a constant uplift rate of 1×10^{-3} m yr^{-1} is prescribed over the entire domain except the boundary nodes. FastScape uses a rectangular domain of 100 km $\times$ 100 km resolved by 384×384 cells, giving a cell size of 0.26 km. The topography is initialized to 0, and random noise is applied. The bedrock erodibility K_f is set to 2×10^{-6} m$^{0.2}$ yr^{-1} and the transport coefficient K_d is set to 1×10^{-1} m^2 yr^{-1}. A constant uplift rate is applied in all domains except the boundaries. All FastScape boundaries are open.

Table 1. The parameters used in NoFSModel.

Materials	Constant viscosity (Pa s)	ρ (kg m^{-3})
Sticky air	1×10^{18}	1
Rigid block	1×10^{24}	3400
Surrounding material	1×10^{21}	3300

3.1.2 Results of the verification tests

We ran the NoFSModel in two configurations, coupled (FastScape + LaMEM) and standalone (only LaMEM). The block descends slightly due to its higher density than the surrounding material, producing a basin above the block and

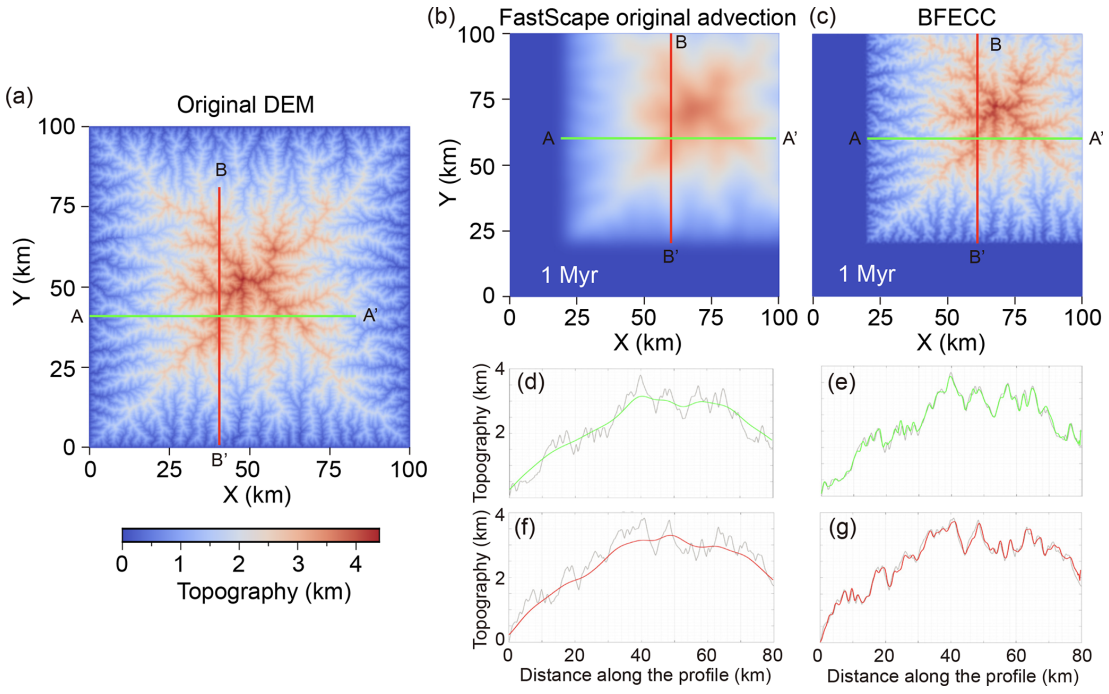


Figure 2. Comparison of the original FastScape advection method and the Back and Forth Error Compensation and Correction (BFECC) method (Liu et al., 2005; Kim et al., 2007). Topography profiles along transect AA' and BB' are presented for the original method in **(d)** and **(f)**, and for the BFECC method in **(e)** and **(g)**, respectively. The grey curves in **(d)**–**(g)** are topography profiles from the original DEM.

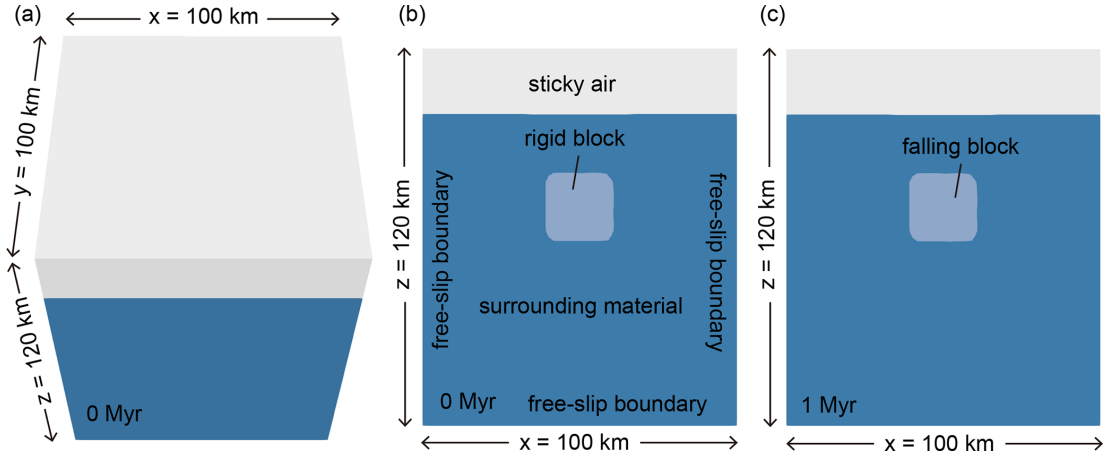


Figure 3. Initial model setup and evolution of the NoFSModel (coupled verification test with negligible erosion). **(a)** 3D view of the initial compositional field. **(b)** Vertical profile at $y = 50$ km. **(c)** Composition field at 1 Myr. The block descends slightly due to its higher density relative to the surrounding material.

a slightly positive topography near the boundary due to isostatic adjustment (Figs. 3c and 4a–b). The two configurations yield nearly identical topography evolution. The maximum absolute topography difference is less than 1 m over 1 Myr, and it is essentially 0 km in most locations (Fig. 4c). This small discrepancy primarily arises from differences in the advection schemes implemented in LaMEM and FastScape: topographic advection is handled by FastScape in the coupled configuration, whereas it is handled by LaMEM in the standalone configuration.

We ran the NoLMModel in two configurations, coupled with the data transfer disabled (FastScape + LaMEM) and standalone (only FastScape). The prescribed uplift generates positive topography that is progressively dissected, and dendritic river networks emerge as the landscape evolves (Fig. 5a–b, e–f). The two configurations yield nearly identical results for the topography evolution and river systems.

Table 2. The parameters used in plume model.

Materials	Constant viscosity (Pa s)	ρ (kg m^{-3})
Sticky air	1×10^{18}	1
Rigid block	1×10^{24}	3200
Surrounding material	1×10^{21}	3300

The maximum topography difference is below 1 cm, with a maximum relative difference below 1×10^{-3} % (Fig. 5c–d). The maximum drainage-area difference is below 1×10^{-3} km^2, with a maximum relative difference below 1×10^{-3} % (Fig. 5g–h).

These results verify that, in the tested decoupled configurations, the coupling interface reproduces the standalone component solutions within the numerical differences associated with the respective advection treatments and data-transfer procedures.

3.2 Plume model

3.2.1 Initial model setup

We next consider the upwelling of a buoyant block, a simple analog for plume-induced doming, to compare a 2D coupled configuration with a fully 3D coupled configuration. Following previous work, we refer to the 2D coupled configuration that the landscape model extends in the second horizontal direction as the T-coupled model (cf. Wolf et al., 2022b). For the 2D thermo-mechanical model, the model domain is 100 km × 120 km in the x-z plane (Fig. 6a), resolved by 192×96 cells, with a buoyant rigid block at 40 to 60 km in the x-direction and -40 to -20 km in the z-direction. For the 3D model, the model domain is 100 km × 100 km × 120 km (Fig. 6c–d), resolved by $96 \times 96 \times 96$ cells, with the block at 40 to 60 km in the x-direction, 40 to 60 km in the y-direction, and -40 to -20 km in the z-direction. All rheological parameters used in these two models are listed in Table 2. These two models are free-slip for all boundaries except the free-surface top boundary. A 20 km-thick "sticky-air" layer is used to mimic the internal free-surface condition in the finite difference scheme. The side boundaries have zero heat flux.

In the T-coupled model, the y-direction is extended to 100 km in FastScape. The resolution (384×384 cells, 0.26 km) is finer than that of the thermo-mechanical model. For the 3D coupled model, FastScape uses the same surface domain (100 km × 100 km) with a resolution of 192×192 cells (0.52 km spacing). Both configurations use the same surface parameters: stream power exponents are set to $m = 0.4$ and $n = 1.0$ (Yuan et al., 2019; 2022). All boundaries are open.

3.2.2 Comparison of the T-coupled and fully 3D models

Both configurations develop an uplift of approximately 100–200 m above the block, surrounded by a slight depression due to isostatic adjustment (Fig. 7a–b). The T-coupled model produces a linear ridge with a larger topographic amplitude (Fig. 7c) because the 2D thermo-mechanical solution cannot spread the buoyant upwelling in the y-direction (Fig. 7a). In contrast, the 3D model captures the dome-shaped landscape (Fig. 7b). The river networks exhibit different patterns accordingly. In the T-coupled model, rivers drain the ridge on both flanks in nearly parallel, x-oriented catchments, whereas in the 3D model, rivers form a radial pattern centered on the dome (Fig. 7d–e).

3.2.3 Parameter variations

We investigate the effects of thermo-mechanical parameters (density contrast between the surrounding materials and the rigid block ($\Delta\rho$)) and the surface parameters (bedrock erodibility K_f and transport coefficient K_d) on the 3D plume models. The purpose of these tests is to demonstrate that the coupled model remains stable and produces physically consistent results across the parameter ranges relevant to applications, not to derive geodynamic conclusions.

$\Delta\rho$ directly influences the upwelling rate of the block. A higher $\Delta\rho$ results in a more pronounced dome-shaped landscape and an increased number of river systems (Fig. 8a–c). K_f significantly impacts the erosional rate. When K_f is set to 1×10^{-7} m$^{0.2}$ yr^{-1}, erosion is minimal, leading to changes in river shape, including bends occurring near the dome (Fig. 8d). Conversely, when K_f is increased to 1×10^{-5} m$^{0.2}$ yr^{-1}, the dome experiences substantial erosion, and its elevation approaches 0 km (Fig. 8f). The K_d directly affects the hillslope processes and the smoothness of the topography. With lower K_d values of 1×10^{-2} or 1×10^{-4} m^2 yr^{-1}, the topography becomes rougher, and several river systems begin to emerge (Fig. 8g–h). However, with a higher K_d value of 1 m^2 yr^{-1}, the topography remains very smooth, and no significant large river systems develop (Fig. 8i).

In all cases, the coupled model runs stably, and the topographic and drainage responses follow the expected physical trends, indicating that the module behaves reliably across the tested parameter space.

3.3 Subduction model

3.3.1 Initial model setup

Oceanic subduction is a fundamental process in plate tectonics. In this section, we establish a simple 3D thermo-mechanical-geomorphological model to demonstrate the effectiveness of the coupling module. The model domain is 800 km × 200 km × 415 km (Fig. 9), resolved by the Eulerian mesh of $384 \times 96 \times 96$ cells. The model is composed of

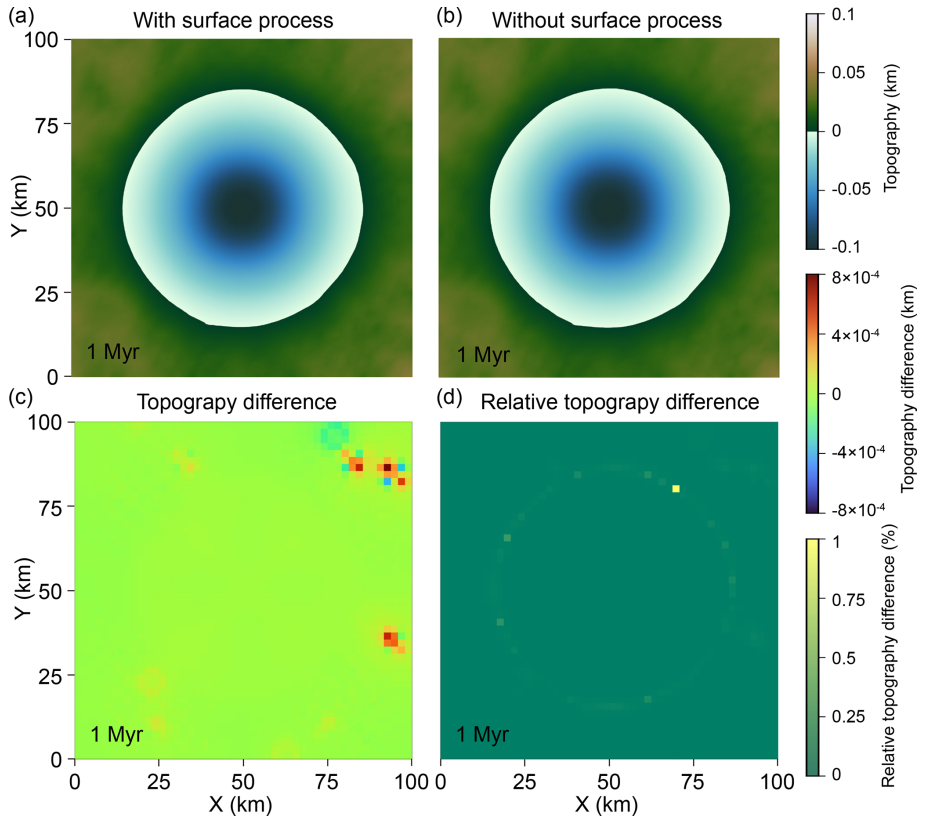


Figure 4. Verification test of the NoFSModel against standalone LaMEM. Surface topography at 1 Myr for **(a)** the coupled run with negligible erosion and **(b)** the standalone LaMEM run without the coupling module. **(c)** Topography difference between **(a)** and **(b)**. **(d)** Relative topography difference. The color scale for the topography field is from Crameri (2023).

a 400 km-long left ocean, which includes a 100 km × 100 km oceanic plateau, and a 400 km-long right overriding ocean. All oceans comprise an 8 km-thick crust and a 90 km-thick lithospheric mantle. The oceanic plateau comprises a 20 km-thick crust and a 78 km-thick lithospheric mantle. All rheological parameters are listed in Tables 3 and 4. The model is free-slip for all boundaries except the free-surface top boundary. A 15 km-thick "sticky-air" layer is used to mimic the internal free-surface condition in the finite difference scheme. We apply a constant pushing velocity on the subducting plate (5 cm yr^{-1}). A 15 km-thick weak zone between the subducting and overriding plate is used to initiate the subduction. The side boundaries have zero flux, and a linear temperature profile is employed with fixed temperatures of 0 °C at the surface and 1500 °C at the bottom. A linear strain weakening of the internal friction angle is used in the model, which linearly decreases by 90 % between strains of 0.01 and 0.05.

FastScape has the same domain as the tectonic model's plane (800 km × 200 km), and the resolution is finer than the thermo-mechanical (2304 × 576 cells) model. The stream power exponents are set to $m = 0.4$ and $n = 1.0$ (Yuan et al., 2019, 2022). All boundaries are open, allowing flux to pass.

3.3.2 Evolution of the subduction model

Under continuous convergence force, the subducting oceanic slab continues to descend beneath the overlying plate. In the early stages of subduction, the presence of oceanic plateaus leads to the formation of elevated topography at their locations. The contour lines of this topography bend toward the subduction zone, causing rivers in the area to adjust accordingly and exhibit a similar pattern of curvature (Fig. 10a). As the subduction proceeds and parts of the oceanic plateau enter the subduction channel, the overlying elevation decreases, and the previously curved rivers begin to straighten out (Fig. 10b).

4 Discussion

4.1 Verification, numerical robustness, and computational performance

The decoupled end-member tests indicate that the coupling module reproduces the solutions of the component codes within the numerical differences expected from the tested interface and advection treatments. These tests validate the

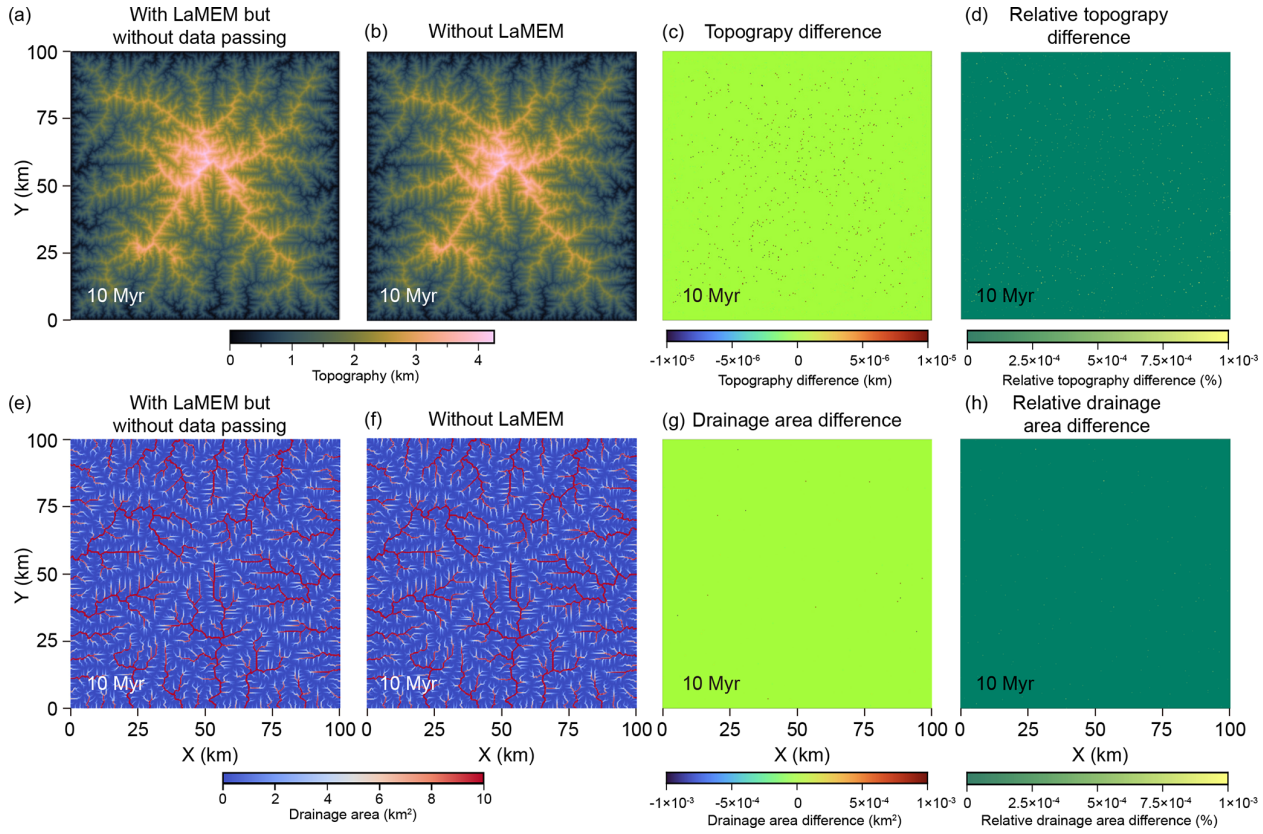


Figure 5. Verification test of the NoLMModel against standalone FastScape. **(a, b)** Topography and **(e, f)** drainage area at 10 Myr for the coupled run without data transfer from LaMEM **(a, e)** and the standalone FastScape run **(b, f)**. **(c, d)** Topography difference and relative topography difference. **(g, h)** Drainage area difference and relative drainage area difference.

Table 3. The rheological parameters used in numerical models.

Notation	Rheology	E (kJ mol^{-1})	V (cm^3 mol^{-1})	n	B_N (Pa^{-n} s^{-1})
A	Isoviscous	0	0	1	5×10^{-19}
B	Wet Quartzite[a]	154	0	2.3	1.55×10^{-17}
C	Dry olivine[b]	530	15	3.5	6.22×10^{-16}
		375	5	1	1.5×10^{-9}
D	Isoviscous	0	0	1	5×10^{-20}

Flow laws used in numerical models are from experimental data: [a] Ranalli (1995), [b] Hirth and Kohlstedt (2003).

data-transfer pathways for the two decoupled end-member configurations, but they should not be interpreted as a complete assessment of interpolation and advection errors in fully coupled simulations. Such errors may become more important when strong spatial gradients, large velocity variations, refined surface grids, or rapidly changing tectonic forcing are present. The coupled configurations match the standalone LaMEM and FastScape results to within 1 m and 1 cm of topography, respectively, with relative differences below 10^{-3} % (Figs. 4 and 5). These tests verify the implementation at the interface level, which is the component this paper introduces, while the numerical solvers of LaMEM and FastScape have been verified in their original publications (Braun and Willett, 2013; Kaus et al., 2016; Yuan et al., 2019). In particular, the tests demonstrate consistency when either surface processes forcing or thermo-mechanical data transfer is effectively inactive. The plume-model parameter tests provide a measure of numerical robustness. The parameter sensitivity tests further show that the coupled model remains stable across the tested ranges of buoyancy forcing, erodibility, and

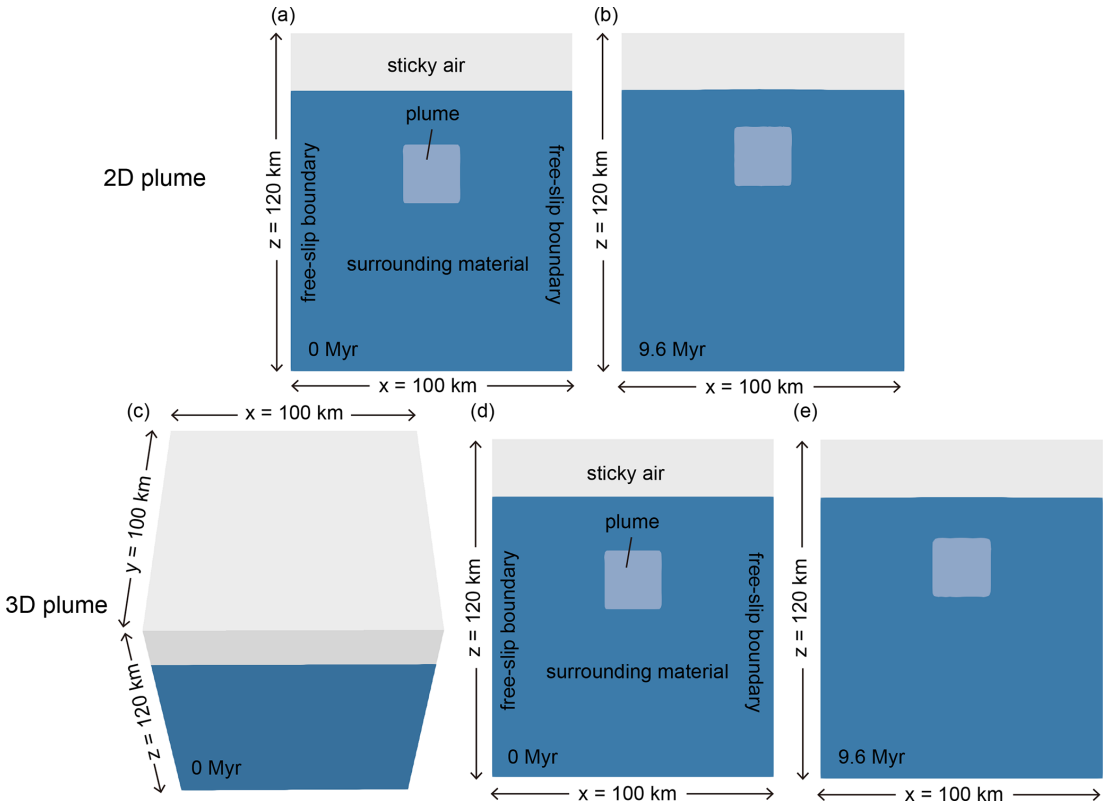


Figure 6. Initial model setup and evolution of the 2D-coupled (T-coupled) and fully 3D-coupled plume model. **(a)** Initial compositional field of the 2D plume model. **(b)** The 2D plume model at 9.6 Myr. **(c)** 3D view of the compositional field of the 3D plume model. **(d)** The vertical profile at $y = 50$ km of the 3D plume model. **(e)** The evolution of the 3D plume model at 9.6 Myr.

Table 4. Main material parameters in subduction model.

Materials	ρ (kg m^{-3})	C (MPa)	ϕ (°)	K (W m^{-1} K^{-1})	H_r (W kg^{-1})	Rheology
Oceanic crust	2900	1	5	3.0	3×10^{-11}	B
Lithospheric mantle of oceans	3300	10	30	3.5	6×10^{-12}	C
Sublithospheric mantle	3300	10	30	3.5	6×10^{-12}	C
Air	1	–	–	100	0	A
Weak zone	3200	–	–	3	0	D

For all rock types, the thermal expansivity $\alpha = 3 \times 10^{-5}$ K^{-1}, compressibility $\beta = 1 \times 10^{-11}$ Pa^{-1}, heat capacity $C_p = 1200$ J kg^{-1}.

hillslope diffusivity, and that the topographic and drainage responses follow the expected physical trends (Fig. 8). The resolution experiments further show that the organization of the drainage network depends strongly on the FastScape grid spacing, emphasizing the need for model-specific resolution tests before interpreting individual channels or drainage divides.

The computational cost of the coupling module primarily arises from gathering surface node information on the primary MPI rank, interpolating between LaMEM and FastScape grids, executing the serial landscape calculation, and returning the updated topography to LaMEM. This overhead increases with the number of nodes and ranks. For example, in the 3D plume model, which has dimensions of $100 \times 100 \times 100$ km, is resolved with $96 \times 96 \times 96$ cells, and is run on 64 cores, the total solution time is 989 s. In comparison, the solution time for LaMEM is 610 s, for FastScape it is 244 s, and for the coupling module, it takes 135 s. This means the coupling module accounts for 13.7 % of the total solution time. In the case of the 3D subduction model, which spans $800 \times 200 \times 415$ km and is resolved with $384 \times 96 \times 96$ cells, calculated on 256 cores, the total solution time is 10,561 s. By comparison, the solution time for LaMEM is 8411 s, for FastScape is 1928 s, and for the coupling module is 222 s. Here, the coupling module represents only 2.1 % of the total solution time. Because the thermo-mechanical cost grows

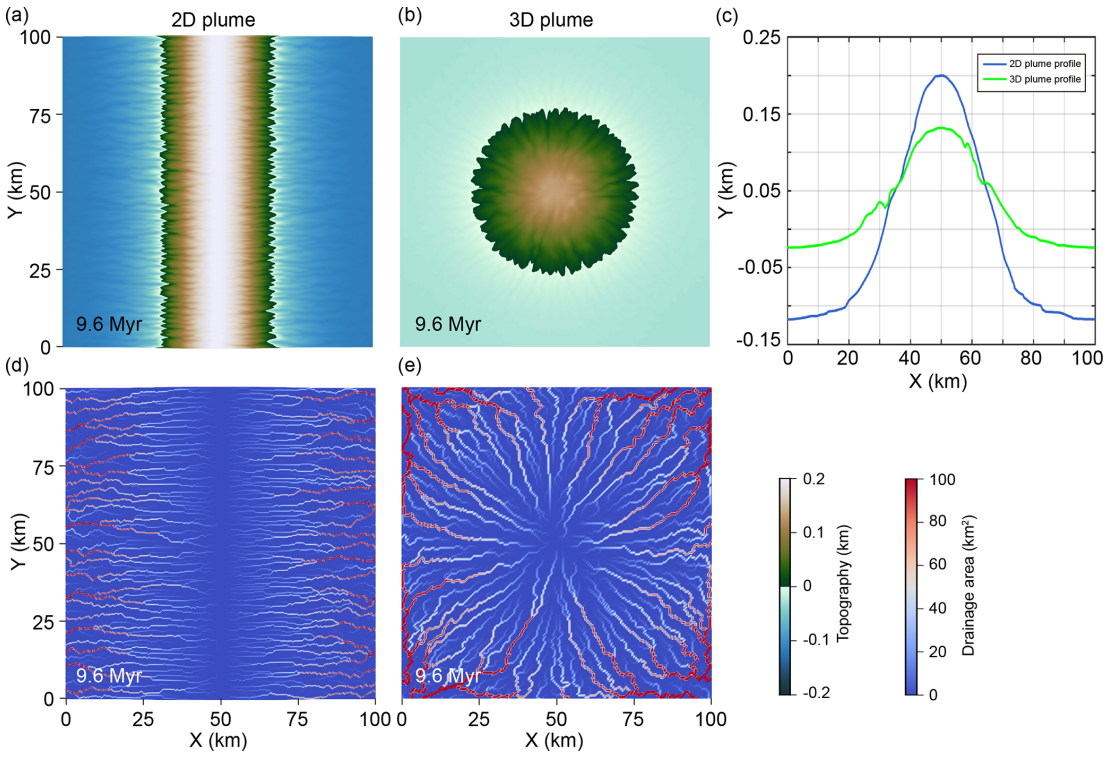


Figure 7. Comparison of T-coupled and fully 3D-coupled plume models at 9.6 Myr. **(a, d)** Topography and drainage area of the T-coupled model. **(b, e)** Topography and drainage area of the fully coupled 3D model. **(c)** The topography profile of the 2D and 3D plume models at $y = 50$ km. The T-coupled model produces a linear ridge with parallel drainage, whereas the 3D model produces a dome with radial drainage.

with the full 3D problem size while the coupling cost grows only with the surface grid, the relative overhead decreases for larger applications.

4.2 The role and scope of fully 3D coupling

Based on our tests of 2D and 3D plumes, the T-coupled model cannot fully replace the 3D model when there is a significant horizontal variation in the extended horizontal direction. The T-coupled model shows uniform evolution in the extended direction and only captures the results along a specific profile, rather than representing the entire results across the x-y plane (Fig. 7). However, the T-coupled configuration remains useful for problems in which the thermo-mechanical structure and forcing are approximately invariant in the extended horizontal direction, including subduction or continental extension. It retains the lower computational cost of a two-dimensional thermo-mechanical model while allowing the development of a two-dimensional drainage network on the surface. Such models may be appropriate when the principal objective is to examine the evolution of a representative tectonic cross-section, and along-strike variability is not central to the scientific question. However, because the thermo-mechanical solution is identical along the extended direction, T-coupled models cannot generate dynamically evolving lateral variations in uplift, deformation, or surface velocity. For example, in the subduction model, the oceanic plateau introduces an along-strike contrast in uplift, erosion, and river organization that has no 2D representation at all, although this model is still simplified compared to a particular natural subduction zone (Fig. 10). Applications in which the surface response to laterally varying tectonic structure matters, such as drainage reorganization above growing domes, slab-related lateral relief, or fault-controlled landscapes, therefore require the fully 3D coupling.

4.3 Surface advection and grid transfer

The coupling module transfers fields between grids and advects topography over landscape substeps. Here, we examine the effects of the surface-advection treatment and discuss limitations associated with grid transfer and spatial resolution.

4.3.1 Comparison of surface advection treatments

We compare two treatments of surface advection using NoFSModel simulations (Fig. 11). In the first treatment, LaMEM advects the topography once per thermo-mechanical timestep, after which FastScape advances the surface processes with negligible erosion and diffusion. In the second treatment, topographic advection is performed

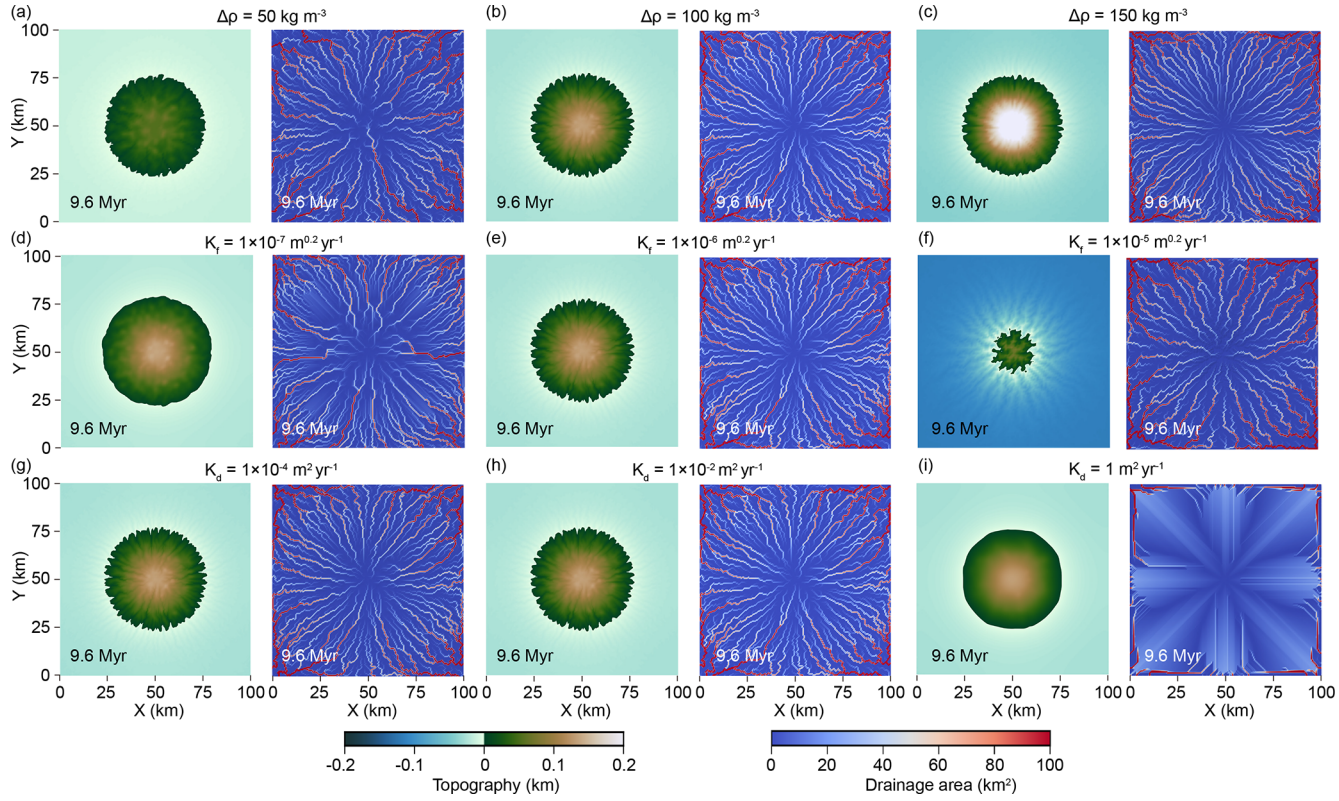


Figure 8. Parameter sensitivity tests of the 3D plume models. Each panel shows topography (left) and drainage area (right) at 9.6 Myr. **(a–c)** Density contrast $\Delta\rho = 50$, 100, 150 kg m^{-3}. **(d–f)** Bedrock erodibility $K_f = 1 \times 10^{-7}$, 1×10^{-6}, 1×10^{-5} m$^{0.2}$ yr^{-1}. **(g–i)** Transport coefficient $K_d = 1 \times 10^{-4}$, 1×10^{-2}, 1 m^2 yr^{-1}. In each series, the remaining parameters are held at the reference values ($\Delta\rho = 100$, $K_f = 1 \times 10^{-6}$ m$^{0.2}$ yr^{-1}, $K_d = 1 \times 10^{-2}$ m^2 yr^{-1}).

within the FastScape landscape substeps. Each calculation is compared with standalone LaMEM using the same physical setup and density contrast.

The results of the first treatment are shown in Fig. 11a–c. Under the tested configuration, the maximum topographic difference is 5×10^{-12} km, and the relative topographic difference does not exceed 2.5×10^{-9}. Under the tested configuration, this advection treatment reproduces the standalone LaMEM topography to within the reported numerical difference, implying that the other parts of the coupling module work well. The second treatment conducts self-consistent advective and erosive deposition processes in FastScape. Due to differences in the advection scheme, a larger topographic difference is expected. This comparison indicates that the choice of advection treatment contributes to the observed topographic differences in the tested configuration. Nevertheless, because no analytical solution exists for this coupled configuration, it is difficult to quantitatively compare true error values across different advection modes.

Despite the close agreement with the standalone LaMEM result in the first advection treatment, we use the second advection treatment in the fully coupled simulations. In the first treatment, the full thermo-mechanical displacement is applied at the beginning of the thermo-mechanical timestep, and the topography used by FastScape may become inconsistent with the intermediate topographic state during the subsequent landscape evolution substeps. The second design is more physically consistent for landscape modeling. In this advection mode, each iteration of FastScape runs the advection, erosion, and deposition processes, thereby capturing the bidirectional feedback among erosion, deposition, and uplift at each substep.

4.3.2 Grid-transfer in the coupling module

Due to differences in the grid settings of LaMEM and FastScape, information transfer via interpolation is indispensable. Bilinear interpolation provides a computationally efficient and straightforward means of transferring velocity fields from a structured thermo-mechanical grid to the geomorphic grid. Because it uses the four surrounding source-grid values, it produces a spatially continuous field and generally avoids the grid-scale discontinuities associated with nearest-neighbor interpolation. It is therefore suitable for coupling models with compatible, regular grids when the velocity field varies smoothly at the scale of the interpolation cell. This approach offers a practical way to estimate veloci-

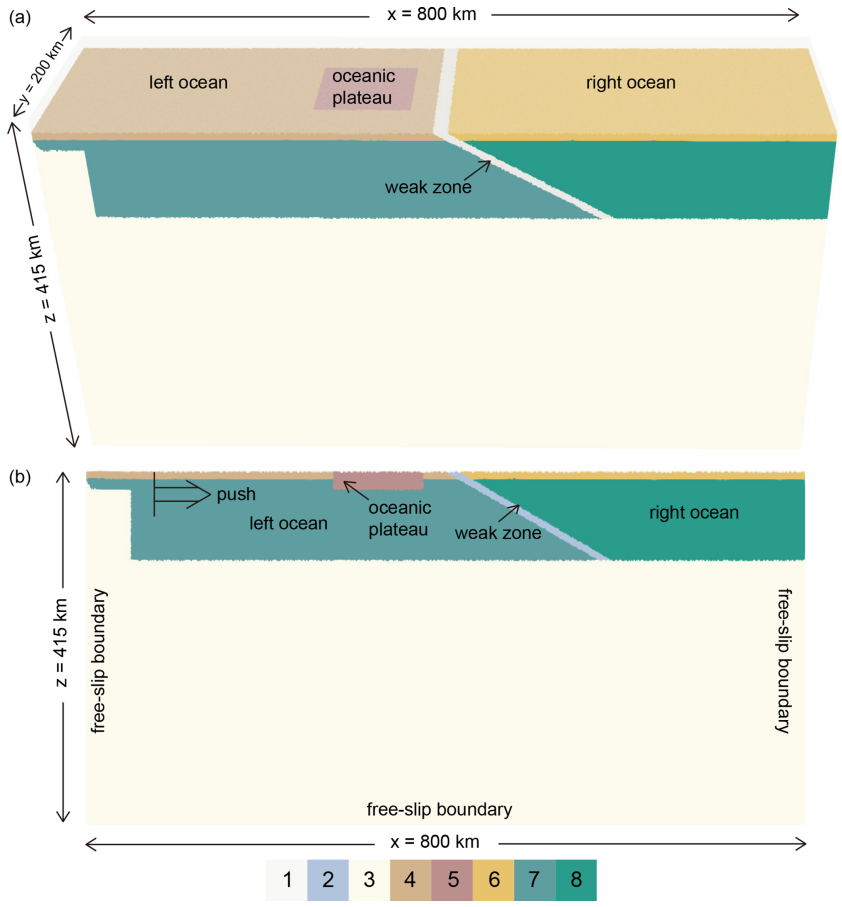


Figure 9. Initial model setup for the subduction model. **(a)** 3D view of the compositional field. **(b)** The vertical profile at $y = 100$ km. 1 – sticky air; 2 – weak zone; 3 – sublithospheric mantle; 4 – oceanic crust of left ocean; 5 – oceanic plateau; 6 – oceanic crust of right ocean; 7 – lithospheric mantle of left ocean; 8 – lithospheric mantle of right ocean. A constant velocity of 5 cm yr^{-1} is applied to the subducting plate.

ties at geomorphic grid nodes without introducing substantial computational overhead.

However, bilinear interpolation does not guarantee conservation of cell-integrated mass or flux, which should be distinguished from the physical loss of sediment through open lateral boundaries. Its smoothing may also attenuate sharp gradients and localized features, including deformation across narrow shear zones or faults, which is most pronounced when the source velocity grid is coarse relative to the geomorphic grid. In addition, interpolation errors can propagate through the advection scheme used by FastScape, potentially amplifying numerical diffusion and dispersion during repeated field exchanges. Although the Back and Forth Error Compensation and Correction method (Liu et al., 2005; Kim et al., 2007) reduces excessive diffusion under nearly uniform horizontal velocities, it cannot fully remove errors caused by velocity interpolation or limited surface-grid resolution.

Several approaches could be considered to reduce or quantify these errors in future work. Conservative remapping would be preferable when transferring quantities for which an integral constraint should be preserved (Cheng and Shu, 2008). Sensitivity experiments involving the interpolation method and surface-grid resolution would provide direct estimates of the retention of local extrema and numerical uncertainty. In addition, dedicated benchmark problems with prescribed velocity fields and known solutions would allow the interpolation and advection errors to be separated from the physical uncertainties of the coupled geodynamic problem. These developments are beyond the scope of the present study, but they define important directions for future improvement of the coupling module.

4.4 Limitations and scope of applicability

The coupled model has several documented limitations, which also define its recommended scope of use.

First, drainage organization is sensitive to the spatial pattern of the imposed tectonic velocity field. In models with nearly uniform horizontal surface motion and homogeneous material structure, the drainage network may inherit the symmetry of the forcing and develop artificially regular or straight channels. Initial topographic perturbations and later-

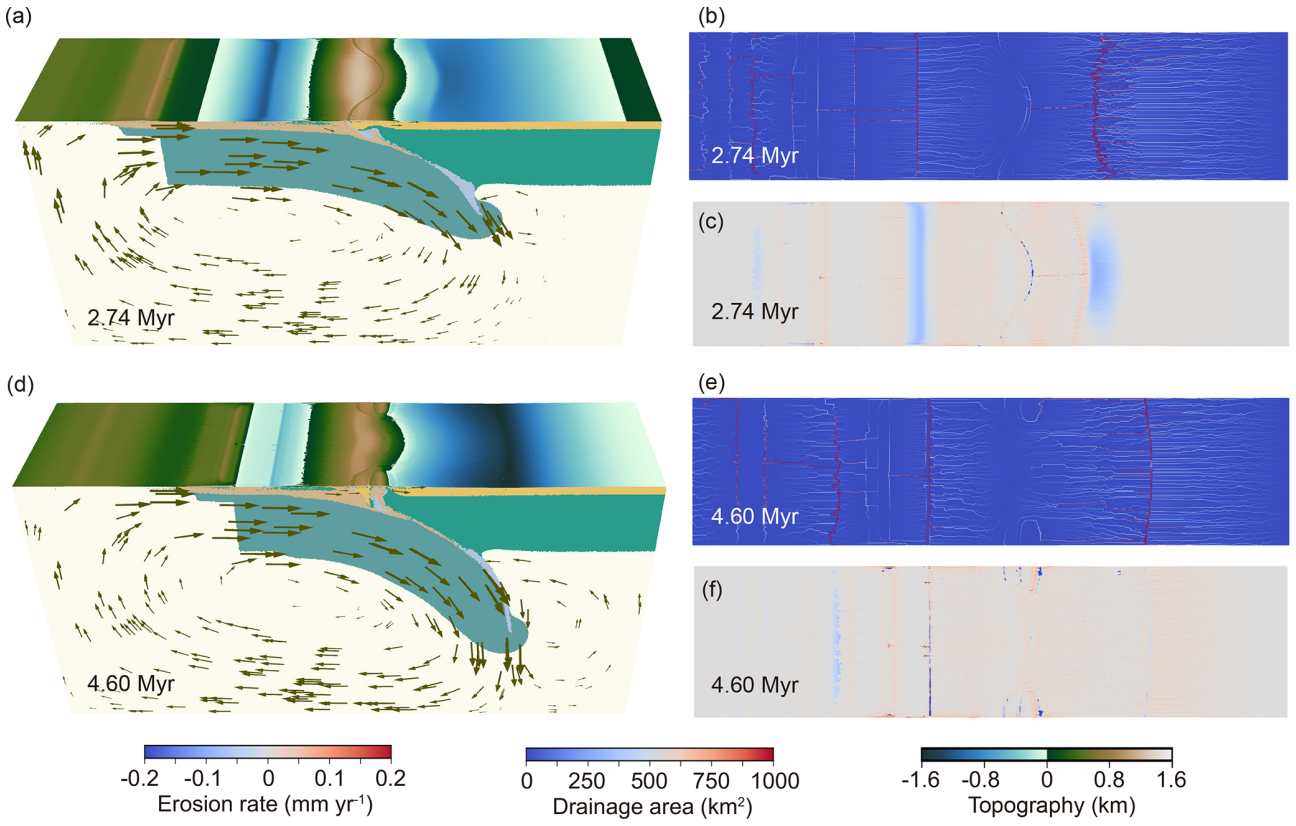


Figure 10. Evolution of the subduction model at two time steps: **(a–c)** 2.74 Myr and **(d–f)** 4.60 Myr. Each panel shows **(a, d)** topography and lithology (colors follow Fig. 9), **(b, e)** drainage area, and **(c, f)** erosion rate. Olive-green arrows indicate the velocity field.

ally variable tectonic forcing are therefore important when the geometry of individual river systems is of interest.

Second, the FastScape grid is generated and remains fixed for the duration of a simulation. The topographic field evolves on this grid, but its node coordinates and connectivity are not dynamically stretched, compressed, or regenerated. This persistence is necessary because the organization of the landscape into valleys and ridges has a response time of up to several Myr, and any regridding artificially resets it. LaMEM configurations that stretch or contract the grid, such as models with a background strain rate, are therefore not supported currently for the coupling.

Third, FastScape executes serially on a single rank. For the surface grids used here, this cost is small (Sect. 4.1). However, for very large or highly refined surface grids, the serial landscape solver and its memory footprint will eventually limit scalability.

Taken together, our tests show that our approach reproduces the standalone component solutions under decoupled end-member scenarios and can be applied to tectonic models with laterally variable surface forcing. This contribution provides the LaMEM community with a documented and reusable interface to FastScape. The plume and subduction examples illustrate the feasibility of this coupling approach. Reliable application of the module requires model-specific assessment of surface resolution, coupling timestep, grid interpolation, and boundary conditions.

5 Conclusions

We have presented a coupling module that connects the 3D thermo-mechanical code LaMEM with the landscape evolution code FastScape. Two decoupled end-member tests verify the implementation, with coupled results matching standalone LaMEM and FastScape solutions to within 1 m and 1 cm of topography, respectively. Parameter sensitivity tests across buoyancy, erodibility, and diffusivity ranges confirm stable operation and physically consistent responses. The coupling overhead is modest, 13.7 % of total solution time in a small 3D plume model and 2.1 % in a larger 3D subduction model, and decreases with problem size. A comparison between a T-coupled configuration and a fully 3D coupled configuration of the same plume model shows that only the 3D coupling captures the dome-shaped uplift and radial drainage, and a 3D subduction model with an oceanic plateau demonstrates the module in a large-scale application with along-strike variability. The source code, input files, and a user manual are openly available (Luo et al., 2026), provid-

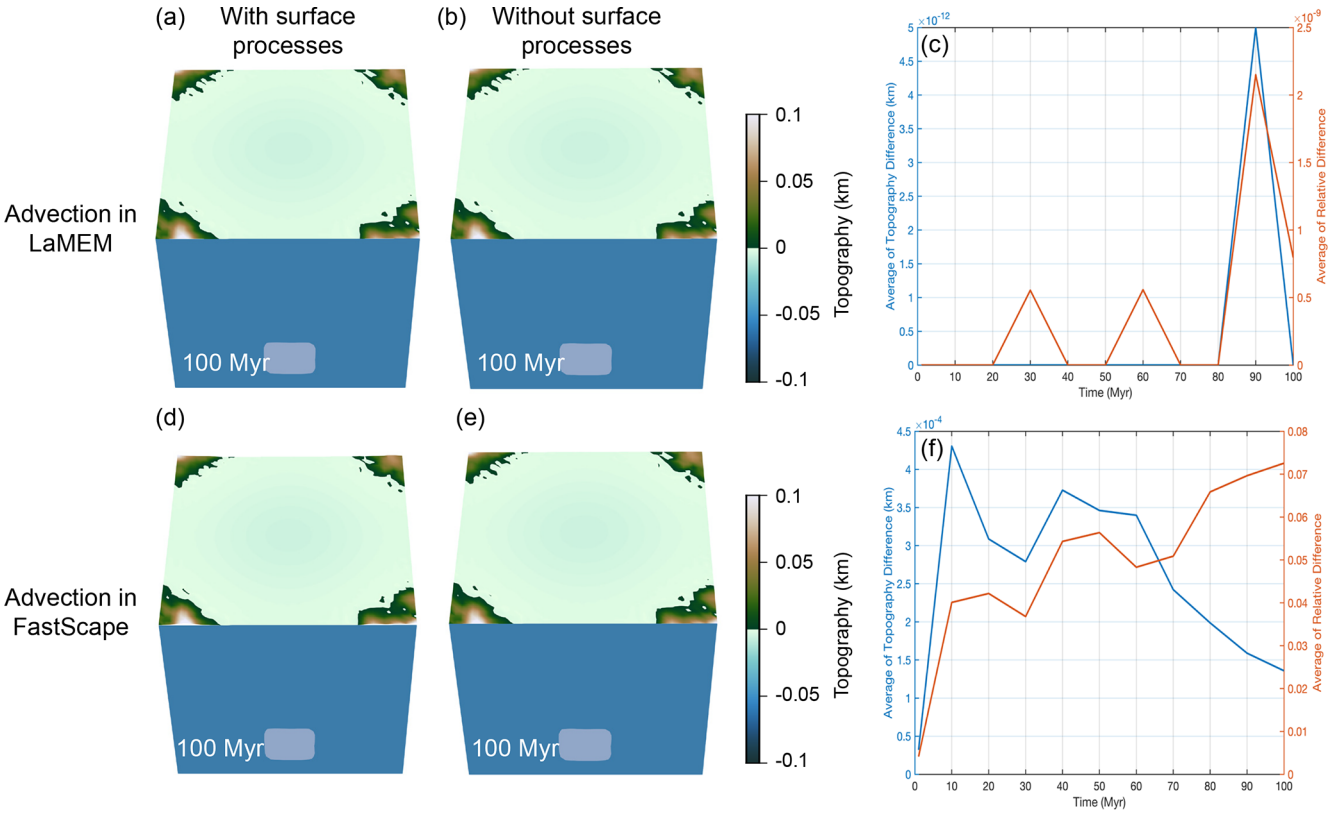


Figure 11. Comparison of model results under the same thermo-mechanical setting, with/without surface processes. **(a–c)** Simulation with topographic advection is performed by LaMEM. **(d–f)** Simulation with advection is performed by FastScape. The blue and red lines in **(c)** and **(f)** are the average of the topography difference and the average of the relative topography difference, respectively.

ing the LaMEM community with a documented and tested tool for exploring feedback between lithospheric deformation and surface processes in three dimensions.

Code availability. The scripts and model inputs reported in this paper are available from Zenodo (https://doi.org/10.5281/zenodo.21761705, Luo et al., 2026) under the Creative Commons Attribution 4.0 International license.

Data availability. No data were used or generated in this study.

Author contributions. With guidance from JFY, BK, AP, XPY, and LZ, LY led the coupling of the model, implementing the representation of thermo-mechanics-surface interactions, model simulations, and results analysis. LY initially drafted the paper, with significant contributions from JFY, BK, AP, XPY, and LZ. SHL helped with the comparison of model results and ran some simulations through another coupling module, ASPECT-FastScape. All co-authors contributed to the paper review and editing.

Competing interests. At least one of the (co-)authors is a member of the editorial board of *Geoscientific Model Development*. The peer-review process was guided by an independent editor, and the authors also have no other competing interests to declare.

Disclaimer. Publisher's note: Copernicus Publications remains neutral with regard to jurisdictional claims made in the text, published maps, institutional affiliations, or any other geographical representation in this paper. The authors bear the ultimate responsibility for providing appropriate place names. Views expressed in the text are those of the authors and do not necessarily reflect the views of the publisher.

Acknowledgements. The authors thank three anonymous reviewers and two editors for their constructive comments, which helped us improve this study.

Financial support. This study was supported by the National Natural Science Foundation of China (42488201), the Strategy Priority Research Program (Category B) of the Chinese Academy of Sciences (XDB0710000), the National Key R&D Program of China

(2025YFF0811502), and the Major Science and Technology Project (CAS).

Review statement. This paper was edited by Mauro Cacace and reviewed by two anonymous referees.

References

Andrés-Martínez, M., Pérez-Gussinyé, M., Armitage, J., and Morgan, J. P.: Thermomechanical implications of sediment transport for the architecture and evolution of continental rifts and margins, Tectonics, 38, 641–665, https://doi.org/10.1029/2018TC005346, 2019.

Avouac, J. P. and Burov, E. B.: Erosion as a driving mechanism of intracontinental mountain growth, J. Geophys. Res.-Sol. Ea., 101, 17747–17769, https://doi.org/10.1029/96JB01344, 1996.

Beaumont, C., Jamieson, R. A., Nguyen, M. H., and Lee, B.: Himalayan tectonics explained by extrusion of a low-viscosity crustal channel coupled to focused surface denudation, Nature, 414, 738–742, https://doi.org/10.1038/414738a, 2001.

Bettinelli, P., Avouac, J. P., Flouzat, M., Bollinger, L., Ramillien, G., Rajaure, S., and Sapkota, S.: Seasonal variations of seismicity and geodetic strain in the Himalaya induced by surface hydrology, Earth Planet. Sc. Lett., 266, 332–344, https://doi.org/10.1016/j.epsl.2007.11.021, 2008.

Bishop, P.: Long-term landscape evolution: linking tectonics and surface processes, Earth Surf. Proc. Land., 32, 329–365, https://doi.org/10.1002/esp.1493, 2007.

Borgohain, B., Mathew, G., Salvi, D., Harbola, D., and Rai, P.: Spatial-temporal variation in erosion rate of Lohit Bomi-Chayu Batholith around eastern Himalayan Syntaxis (SE of the Namche Barwa Massif), Tectonics, 44, e2024TC008507, https://doi.org/10.1029/2024TC008507, 2025.

Braun, J. and Willett, S. D.: A very efficient O(N), implicit and parallel method to solve the stream power equation governing fluvial incision and landscape evolution, Geomorphology, 180, 170–179, https://doi.org/10.1016/j.geomorph.2012.10.008, 2013.

Braun, J. and Yamato, P.: Structural evolution of a three-dimensional, finite-width crustal wedge, Tectonophysics, 484, 181–192, https://doi.org/10.1016/j.tecto.2009.08.032, 2010.

Braun, J.: The many surface expressions of mantle dynamics, Nat. Geosci., 3, 825–833, https://doi.org/10.1038/ngeo1020, 2010.

Burov, E.: Coupled lithosphere-surface processes in collision context, Thrust Belts and Foreland Basins, 3–40, https://doi.org/10.1007/978-3-540-69426-7_1, 2007.

Burov, E. and Cloetingh, S.: Erosion and rift dynamics: new thermomechanical post-rift evolution of extensional basins, Earth Planet. Sc. Lett., 150, 7–26, https://doi.org/10.1016/S0012-821X(97)00069-1, 1997.

Burov, E. and Gerya, T.: Asymmetric three-dimensional topography over mantle plumes, Nature, 513, 85–89, https://doi.org/10.1038/nature13703, 2014.

Castelltort, S., Goren, L., Willett, S.D., Champagnac, J.-D., Herman, F., and Braun, J.: River drainage patterns in the New Zealand Alps primarily controlled by plate tectonic strain, Nat. Geosci., 5, 744–748, https://doi.org/10.1038/ngeo1582, 2012.

Chen, L., Capitanio, F. A., Liu, L., and Gerya, T. V.: Crustal rheology controls on the Tibetan plateau formation during India-Asia convergence, Nat. Commun., 8, 15992, https://doi.org/10.1038/ncomms15992, 2017.

Cheng, J. and Shu, C. W.: A high order accurate conservative remapping method on staggered meshes., Appl. Numer. Math., 58, 1042–1060, https://doi.org/10.1016/j.apnum.2007.04.015, 2008.

Clark, M. K., Schoenbohm, L. M., Royden, L. H., Whipple, K. X., Burchfiel, B. C., Zhang, X., Tang, W., Wang, E., and Chen, L.: Surface uplift, tectonics, and erosion of eastern Tibet from large-scale drainage patterns, Tectonics, 23, https://doi.org/10.1029/2002TC001402, 2004.

Cloetingh, S. and Willett, S. D.: TOPO-EUROPE: understanding of the coupling between the deep Earth and continental topography, Tectonophysics, 602, 1–14, https://doi.org/10.1016/j.tecto.2013.05.023, 2013.

Collignon, M., Kaus, B., May, D., and Fernandez, N.: Influences of surface processes on fold growth during 3-d detachment folding, Geochem. Geophy. Geosy., 15, 3281–3303, https://doi.org/10.1002/2014GC005450, 2014.

Crameri, F.: Scientific colour maps (Version 8.0.1), Zenodo [code], https://doi.org/10.5281/zenodo.8409685, 2023.

Gao, S. S., Silver, P. G., Linde, A. T., and Sacks, I. S.: Annual modulation of triggered seismicity following the 1992 Landers earthquake in California, Nature, 406, 500–504, https://doi.org/10.1038/35020045, 2000.

Gerya, T. V.: Introduction to numerical geodynamic modelling, 2nd Edn., Cambridge University Press, ISBN 9781107143142, 2019.

Heki, K.: Snow load and seasonal variation of earthquake occurrence in Japan, Earth Planet. Sc. Lett., 207, 159–164, https://doi.org/10.1016/S0012-821X(02)01148-2, 2003.

Hirth, G. and Kohlstedt, D.: Rheology of the upper mantle and the mantle wedge: A view from the experimentalists, Geophys. Monogr., 138, 83–106, 2003.

Kaus, B. J., Mühlhaus, H., and May, D. A.: A stabilization algorithm for geodynamic numerical simulations with a free surface, Phys. Earth Planet. Int., 181, 12-20, https://doi.org/10.1016/j.pepi.2010.04.007, 2010.

Kaus, B. J., Popov, A. A., Baumann, T., Pusok, A., Bauville, A., Fernandez, N., and Collignon, M.: Forward and inverse modelling of lithospheric deformation on geological timescales, Proceedings of NIC Symposium, 48, 978–983, 2016.

Kim, B., Liu, Y., Llamas, I., and Rossignac, J.: Advections with significantly reduced dissipation and diffusion, IEEE T. Vis. Comput. Gr., 13, 135-144, https://doi.org/10.1109/TVCG.2007.3, 2007.

Koons, P. O., Zeitler, P. K., Hallet, B., Shroder, J., and Owen, L. A.: Tectonic aneurysms and mountain building, Treatise on Geomorphology, 5, 318–349, 2013.

Li, K., Brune, S., Erdős, Z., Yuan, X., Glerum, A., Berndt, C., and Haas, P.: Pre-rift orogenic erosion facilitates the exhumation of lower crust at rifted margins, Geophys. Res. Lett., 52, e2024GL113543, https://doi.org/10.1029/2024GL113543, 2025.

Liu, C., Linde, A. T., and Sacks, I. S.: Slow earthquakes triggered by typhoons, Nature, 459, 833–836, https://doi.org/10.1038/nature08042, 2009.

Liu, Y., Kim, B., Rossignac, J., and Llamas, I.: Flowfixer: Using BFECC for fluid simulation, in: GVU Technical Report Series, GIT-GVU-05-24, 2005.

Lu, N., Moresi, L., and Giordani, J.: A novel ALE scheme with the internal boundary for true free surface simulation in geodynamic models, Geosci. Model Dev., 19, 5191–5206, https://doi.org/10.5194/gmd-19-5191-2026, 2026.

Luo, Y., Yang, J., Kaus, B. J. P., Popov, A. A., Liu, S., Yuan, X., and Zhao, L.: The source code of the coupling module and input files (1.0.0), Zenodo [code], https://doi.org/10.5281/zenodo.21761705, 2026.

Maiti, G., Koptev, A., Baville, P., Gerya, T., Crosetto, S., and Andrić-Tomašević, N.: Topography response to horizontal slab tearing and oblique continental collision: Insights from 3D thermomechanical modelling, J. Geophys. Res.-Sol. Ea., 129, e2024JB029385, https://doi.org/10.1029/2024JB029385, 2024.

Molnar, P., England, P., and Martinod, J.: Mantle dynamics, uplift of the Tibetan Plateau, and the Indian monsoon, Rev. Geophys., 31, 357–396, https://doi.org/10.1029/93RG02030, 1993.

Moresi, L., Quenette, S., Lemiale, V., Meriaux, C., Appelbe, B., and Mühlhaus, H. B.: Computational approaches to studying non-linear dynamics of the crust and mantle, Phys. Earth Planet. Int., 163, 69–82, https://doi.org/10.1016/j.pepi.2007.06.009, 2007.

Moulas, E., Kaus, B., and Jamtveit, B.: Dynamic pressure variations in the lower crust caused by localized fluid-induced weakening, Commun. Earth Environ., 3, 157, https://doi.org/10.1038/s43247-022-00478-7, 2022.

Munch, J., Ueda, K., Schnydrig, S., May, D. A., and Gerya, T. V.: Contrasting influence of sediments vs surface processes on retreating subduction zones dynamics, Tectonophysics, 836, 229410, https://doi.org/10.1016/j.tecto.2022.229410, 2022.

Neuharth, D., Brune, S., Glerum, A., Morley, C. K., Yuan, X., and Braun, J.: Flexural strike-slip basins, Geology, 50, 361–365, https://doi.org/10.1130/G49351.1, 2022.

Olive, J.-A., Behn, M. D., and Malatesta, L. C.: Modes of extensional faulting controlled by surface processes, Geophys. Res. Lett., 41, 6725–6733, https://doi.org/10.1002/2014GL061507, 2014.

Peaceman, D. W. and Rachford Jr., H. H.: The numerical solution of parabolic and elliptic differential equations, J. Soc. Ind. Appl. Math., 3, 28–41, https://doi.org/10.1137/0103003, 1955.

Popov, A. A. and Sobolev, S. V.: Slim3d: A tool for three-dimensional thermomechanical modeling of lithospheric deformation with elasto-visco-plastic rheology, Phys. Earth Planet. Int., 171, 55–75, https://doi.org/10.1016/j.pepi.2008.03.007, 2008.

Popov, A. A., Berlie, N., and Kaus, B. J. P.: A dilatant visco-elasto-viscoplasticity model with globally continuous tensile cap: stable two-field mixed formulation, Geosci. Model Dev., 18, 7035–7058, https://doi.org/10.5194/gmd-18-7035-2025, 2025.

Pusok, A. E. and Kaus, B. J.: Development of topography in 3-D continental-collision models, Geochem. Geophy. Geosy., 16, 1378–1400, https://doi.org/10.1002/2015GC005732, 2015.

Pusok, A. E., Kaus, B. J. P., and Popov, A. A.: The effect of rheological approximations in 3-D numerical simulations of subduction and collision, Tectonophysics 746, 296–311, https://doi.org/10.1016/j.tecto.2018.04.017, 2018.

Ranalli, G.: Rheology of the Earth, Springer Science & Business Media, ISBN 9780412546709, 1995.

Replumaz, A., San José, M., Margirier, A., van Der Beek, P., Gautheron, C., Leloup, P.H., Ou, X., Kai, C., Wang, G. C., Zhang, Y. Z., and Valla, P. G.: Tectonic control on rapid late Miocene – quaternary incision of the Mekong River Knick-zone, southeast Tibetan Plateau, Tectonics, 39, e2019TC005782, https://doi.org/10.1029/2019TC005782, 2020.

Sacek, V., Braun, J., and van der Beek, P.: The influence of rifting on escarpment migration on high elevation passive continental margins, J. Geophys. Res.-Sol. Ea., 117, https://doi.org/10.1029/2011JB008547, 2012.

Simpson, G. D.: Modelling interactions between fold–thrust belt deformation, foreland flexure and surface mass transport, Basin Res., 18, 125–143, https://doi.org/10.1111/j.1365-2117.2006.00287.x, 2006.

Stanković, N., Gerya, T., Cvetkov, V., and Cvetković, V.: Did the Western and the Eastern Vardar ophiolites originate through a single intra-oceanic subduction? Insight from numerical modelling, Gondwana Res., 124, 124–140, https://doi.org/10.1016/j.gr.2023.07.005, 2023.

Steer, P., Simoes, M., Cattin, R., and Shyu, J. B. H.: Erosion influences the seismicity of active thrust faults, Nat. Commun., 5, 5564, https://doi.org/10.1038/ncomms6564, 2014.

Stock, J. D. and Dietrich, W. E.: Erosion of steepland valleys by debris flows, Geol. Soc. Am. Bull., 118, 1125–1148, https://doi.org/10.1130/B25902.1, 2006.

Sun, B., Kaus, B. J. P., Yang, J., Lu, G., Wang, X., Wang, K., and Zhao, L.: Subduction Polarity Reversal Triggered by Oceanic Plateau Accretion: Implications for Induced Subduction Initiation, Geophys. Res. Lett. 48, e2021GL095299, https://doi.org/10.1029/2021GL095299, 2021.

Theunissen, T. and Huismans, R. S.: Long-term coupling and feedback between tectonics and surface processes during non-volcanic rifted margin formation, J. Geophys. Res.-Sol. Ea., 124, 12323–12347, https://doi.org/10.1029/2018JB017235, 2019.

Thielmann, M., Kaus, B. J., and Popov, A. A.: Lithospheric stresses in Rayleigh–Benard convection: effects of a free surface and a viscoelastic Maxwell rheology, Geophysical Supplements to the Monthly Notices of the Royal Astronomical Society, 203, 2200–2219, https://doi.org/10.1093/gji/ggv436, 2015.

Thieulot, C., Steer, P., and Huismans, R. S.: Three-dimensional numerical simulations of crustal systems undergoing orogeny and subjected to surface processes, Geochem. Geophy. Geosy., 15, 4936–4957, https://doi.org/10.1002/2014GC005490, 2014.

Ueda, K., Willett, S. D., Gerya, T., and Ruh, J.: Geomorphological-thermo-mechanical modeling: application to orogenic wedge dynamics, Tectonophysics, 659, 12–30, https://doi.org/10.1016/j.tecto.2015.08.001, 2015.

Vernant, P., Hivert, F., Chery, J., Steer, P., Cattin, R., and Rigo, A.: Erosion-induced isostatic rebound triggers extension in low convergent mountain ranges, Geology, 41, 467–470, https://doi.org/10.1130/G33942.1, 2013.

Wang, X., Kaus, B.J., Yang, J., Wang, K., Li, Y., Chen, L., and Zhao, L.: 3D Geodynamic Models for HP-UHP Rock Exhumation in Opposite-dip Double Subduction-Collision Systems, J. Geophys. Res.-Sol. Ea., 126, e2021JB022326, https://doi.org/10.1029/2021JB022326, 2021.

Whipple, K. X.: The influence of climate on the tectonic evolution of mountain belts, Nat. Geosci., 2, 97–104, https://doi.org/10.1038/ngeo413, 2009.

Willett, S. D.: Orogeny and orography: The effects of erosion on the structure of mountain belts, J. Geophys. Res.-Sol. Ea., 104, 28957–28981, https://doi.org/10.1029/1999JB900248, 1999.

Willett, S. D., McCoy, S. W., Perron, J. T., Goren, L., and Chen, C. Y.: Dynamic reorganization of river basins, Science, 343, 1248765, https://doi.org/10.1126/science.1248765, 2014.

Wolf, L., Huismans, R. S., Wolf, S. G., Rouby, D., and May, D. A.: Evolution of rift architecture and fault linkage during continental rifting: Investigating the effects of tectonics and surface processes using lithosphere-scale 3D coupled numerical models, J. Geophys. Res.-Sol. Ea., 127, e2022JB024687, https://doi.org/10.1029/2022JB024687, 2022a.

Wolf, S. G., Huismans, R. S., Braun, J., and Yuan, X.: Topography of mountain belts controlled by rheology and surface processes, Nature, 606, 516–521, https://doi.org/10.1038/s41586-022-04700-6, 2022b.

Wolf, S. G., Huismans, R. S., Muñoz, J. A., and May, D. A.: Rift linkage and inheritance determine collisional mountain belt evolution, Nat. Commun., 17, 84, https://doi.org/10.1038/s41467-025-66695-8, 2025.

Xue, L., Moucha, R., Scholz, C. A., and Naliboff, J.: Sedimentation and deformation in oblique continental rifts: The role of climate-tectonic interactions, Earth Planet. Sc. Lett., 669, 119565, https://doi.org/10.1016/j.epsl.2025.119565, 2025.

Yang, J., Kaus, B. J., Li, Y., Leloup, P. H., Popov, A. A., Lu, G., Wang, K., and Zhao, L.: Lower crustal rheology controls the development of large offset strike-slip faults during the Himalayan-Tibetan orogeny, Geophys. Res. Lett., 47, e2020GL089435, https://doi.org/10.1029/2020GL089435, 2020b.

Yang, J., Cao, W., Yuan, X., and Yang, J.: Erosion-Driven Isostatic Flow and Crustal Diapirism: Analytical and Numerical Models with Implications for the Evolution of the Eastern Himalayan Syntaxis, Southern Tibet, Tectonics, 42, e2022TC007717, https://doi.org/10.1029/2022TC007717, 2023.

Yang, R., Suhail, H. A., Gourbet, L., Willett, S. D., Fellin, M. G., Lin, X., Gong, J., Wei, X., Maden, C., Jiao, R., and Chen, H.: Early Pleistocene drainage pattern changes in Eastern Tibet: Constraints from provenance analysis, thermochronometry, and numerical modelling, Earth Planet. Sc. Lett., 531, 115955, https://doi.org/10.1016/j.epsl.2019.115955, 2020a.

Yuan, X. P., Braun, J., Guerit, L., Rouby, D., and Cordonnier, G.: A new efficient method to solve the stream power law model taking into account sediment deposition, J. Geophys. Res.-Earth, 124, 1346–1365, https://doi.org/10.1029/2018JF004867, 2019.

Yuan, X. P., Guerit, L., Braun, J., Rouby, D., and Shobe, C. M.: Thickness of fluvial deposits records climate oscillations, J. Geophys. Res.-Sol. Ea., 127, e2021JB023510, https://doi.org/10.1029/2021JB023510, 2022.

Yuan, X., Li, Y., Brune, S., Li, K., Pons, M., and Wolf, S. G.: Coordination between deformation, precipitation, and erosion during orogenic growth, Nat. Commun., 15, 10362, https://doi.org/10.1038/s41467-024-54690-4, 2024.

Zeitler, P. K., Meltzer, A. S., Koons, P. O., Craw, D., Hallet, B., Chamberlain, C. P., Kidd, W. S., Park, S. K., Seeber, L., Bishop, M., and Shroder, J.: Erosion, Himalayan geodynamics, and the geomorphology of metamorphism, GSA Today, 11, 4–9, 2001.

Zhou, X., Cao, W., Yang, J., Kaus, B. J. P., Ji, W.-Q., Gordon, S. M., and Zuza, A. V.: Raising the Gangdese Mountains via Subduction of Indian Continental Crust, Not Slab Breakoff, During Subduction to Collision Transition. Tectonics, 45, e2026TC009363, https://doi.org/10.1029/2026TC009363, 2026.